FISEVIER

Contents lists available at ScienceDirect

International Journal of Heat and Mass Transfer

journal homepage: www.elsevier.com/locate/ijhmt





Thermal atomization on superhydrophobic surfaces of varying temperature jump length

Eric D. Lee, Daniel Maynes*, Julie Crockett, Brian D. Iverson

Department of Mechanical Engineering, Brigham Young University Provo, UT 84602, United States

ARTICLE INFO

Keywords: Superhydrophobic Droplet Impingement Atomization Heat transfer Temperature jump length

ABSTRACT

This paper presents an experimental study of drop impingement and thermal atomization on hydrophobic and superhydrophobic (SH) surfaces. Superhydrophobic surfaces having both microscale and nanoscale geometry are considered. Microscale SH surfaces are coated with a hydrophobic coating and exhibit micropillars and cavities which are classified using the surface solid fraction and center to center pitch. The solid fraction and pitch values explored in this study range from 0.05-1.0 and 8-60 μ m respectively. Nanoscale textured surfaces are created by applying a blanket layer of carbon nanotubes. Both types of surfaces are further classified by a temperature jump length (λ_T). All experiments were conducted at We = 85. Results of atomization as a function of time for the impingement event are provided for several surfaces of varying surface geometry, surface temperature, and temperature jump length. Nanoscale SH surfaces are shown to completely suppress atomization at all conditions explored. Results of the maximum atomization that occurred on a given surface are also shown as a function of the surface temperature. The surface temperature at which the maximum atomization occurs varies with surface geometry. Further, the time after impact when the maximum atomization occurs is also a function of the SH surface parameters. In general, the maximum atomization magnitude and the surface temperature at which maximum atomization occurs each decrease with increasing λ_T . Further, the time when maximum atomization occurs increases with increasing λ_T .

1. Introduction

Drop impingement is present in a wide range of applications, including spray cooling, ink jet printing, rain, etc. Superhydrophobic (SH) surfaces can minimize the effect of water exposure on surfaces and enable self-cleaning behavior. In order to better implement SH surfaces in heated environments, it is necessary to understand the dynamics and heat transfer of drop impingement on these surfaces. Many studies have been conducted to increase the depth of knowledge surrounding SH surfaces [1,2]. Studies have shown that the introduction of SH surfaces create desirable traits such as self-cleaning [3], drag reduction [4], and anti-icing [5]. Superhydrophobic surfaces have also been shown to greatly increase the performance of energy production [6,7] and water desalination [8,9].

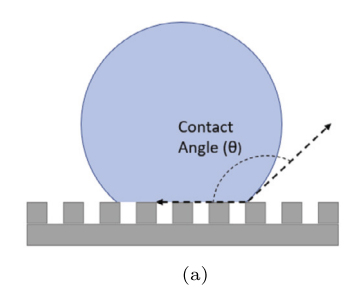
Hydrophobicity, or the degree to which a surface repels water, can be quantified by the static contact angle. The contact angle, illustrated in Fig. 1a, is the angle formed between the surface and the tangent line of the drop at the contact plane. A hydrophilic (HL) surface has a contact angle smaller than 90° , while a smooth hydrophobic (SmH) surface

will have a contact angle greater than 90° . A SH surface has a contact angle that is typically greater than a value of 150° and the contact angle hysteresis is generally smaller than nominally 5° . Superhydrophobic surfaces can be created with either microscale or nanoscale structures. Fig. 2a shows scanning electron microscope (SEM) images of example microscale post (left image) and rib (right image) structured surfaces. Modern manufacturing techniques allow for predefined surface feature dimensions for both microscale post and rib surfaces. Important dimensions of the microstructures are the center-to-center distance between structures (or pitch, w), structure diameter or width (d), and structure height (h), as shown in Fig. 1b and Fig. 2a. One of the most important parameters of a SH surface is the solid fraction (F_s) and it is defined as the ratio of solid surface at the top of the microstructure to the total projected surface area.

Nanoscale textured surfaces can be created by growth of carbon nanotubes (CNT). These structures are not as easily quantified by the parameters listed above for microscale featured surfaces as they are more random in nature, but are often characterized by nanotube height and diameter [10]. Fig. 2b shows an SEM image of carbon nanotubes

E-mail address: maynes@byu.edu (D. Maynes).

^{*} Corresponding author.



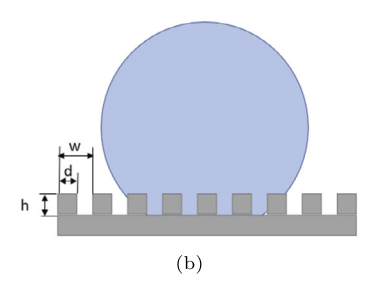


Fig. 1. Drops on microscale structure SH surfaces in the Cassie-Baxter (non-wetting) state (a) and in the Wenzel (wetting) state (b). The microstructure height (h), diameter (d), and pitch (w) are defined as shown, where the post/rib size is exaggerated. For a real scenario there may likely be numerous posts/ribs beneath the drop.

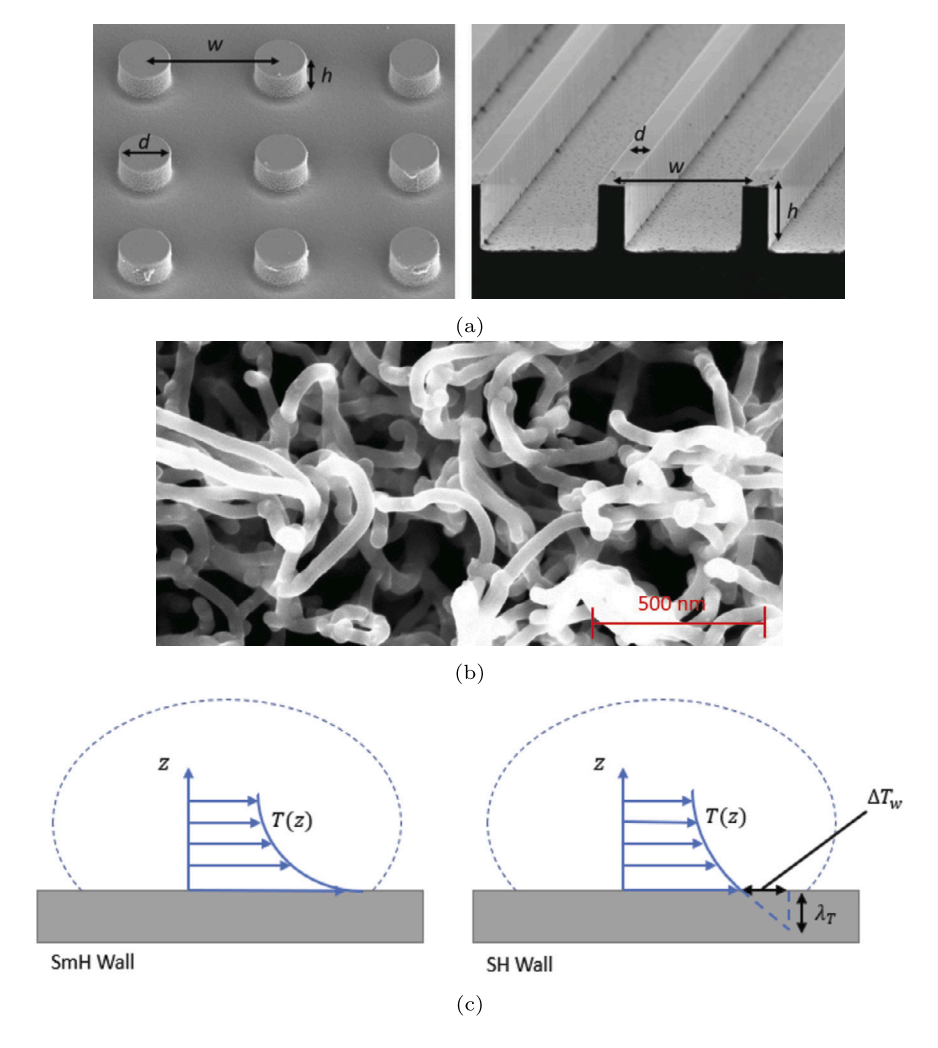


Fig. 2. SEM images of example SH surfaces explored in this work. Panel (a) shows round posts (left) and ribs (right) microscale featured surfaces and the image of panel (b) shows a scan of a nanoscale structured surface using CNTs. Panel (c) illustrates the concept of the temperature jump length, λ_T .

grown on a surface that was used in this study. Note the scale bar that is included at the bottom of the image. After the nanotubes are created, vacuum baking has been shown to yield high levels of hydrophobicity and contact angles as high as 170° have been reported [11,12].

A sessile drop on a SH surface may exist in a Cassie-Baxter state, meaning the liquid does not penetrate the posts or "wet" the surface. A wetted state, also known as the Wenzel state, is also possible but undesirable for high mobility drops. Fig. 1 illustrates the difference between the wetting (Fig. 1b) and non-wetting state (Fig. 1a). Note that the microstructure size is exaggerated in Fig. 1. In reality, numerous structures are present beneath each drop. When the non-wetting state prevails, SH surfaces exhibit a temperature jump at the plane of the top

of the structures on the surface, often characterized by the temperature jump length, λ_T [13–15]. The temperature jump length is illustrated in Fig. 2c and it is analogous to the slip length (λ) presented by Navier [16] and is the distance into the surface that the temperature profile in the drop must be extrapolated to arrive at the surface temperature. For a smooth surface there is no jump in temperature at the wall, but for a SH surface the temperature jump exists due to the fact that the drop is only in contact with the top of each microstructure. This reduction in contact area, combined with the insulating cavities of air between microstructures creates the aggregate effect of the temperature jump. The temperature jump length is analogous to a thermal resistance and, as it increases, the resistance to heat transfer increases as well. It has

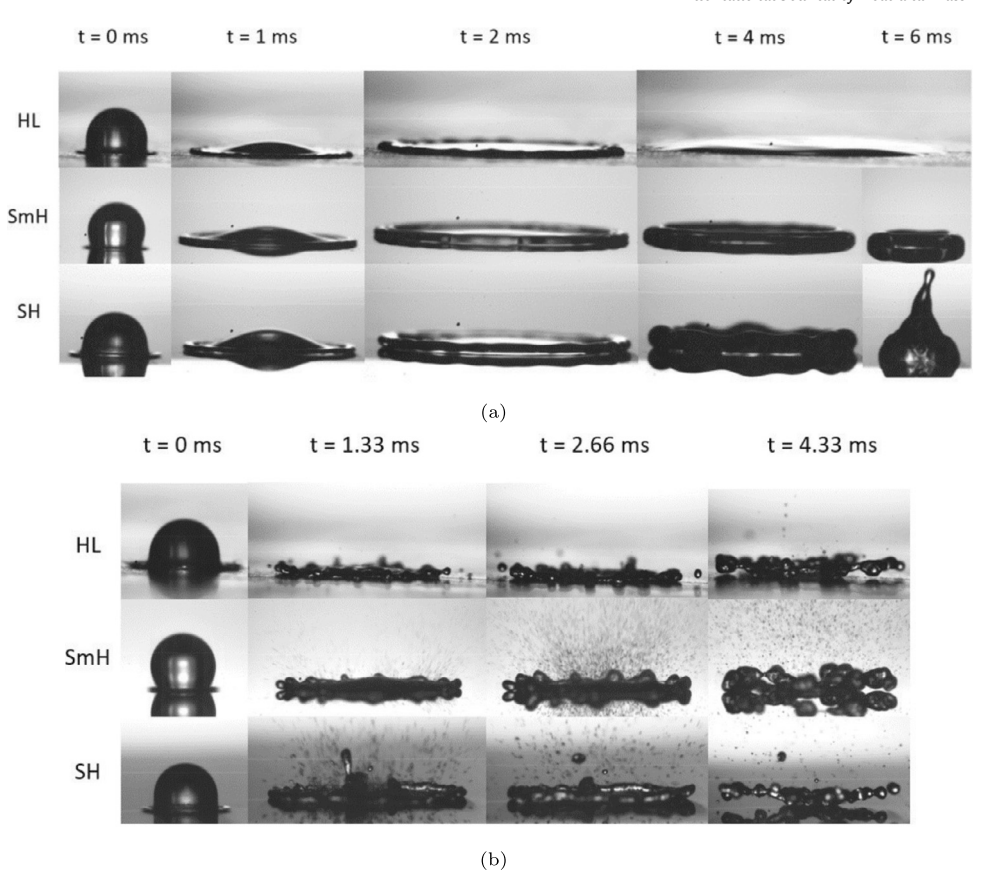


Fig. 3. Temporal progression of impinging drops on hydrophilic (HL), hydrophobic (SmH), and superhydrophobic (SH) surfaces at We = 85 for (a) unheated and (b) superheated surface conditions. The time after initial drop contact with the surface is shown along the top of the images and the surface temperature of the superheated surface was 220 °C.

been shown previously that λ_T can be predicted as a function of the solid fraction and pitch of a SH surface for steady fully-developed laminar microchannel flows. Maynes et al. presented equations for λ_T as a function of the solid fraction, Peclet number, and size of the channel relative to the pitch of the microscale features for flow in channels with SH walls exhibiting transverse [13] and streamwise ribs [14]. Cowley et al. considered the scenario of laminar flow through a microchannel with post structured SH walls and they presented an equation to predict λ_T for this scenario in terms of the governing variables [15]. In general, microchannel heat transfer decreases with increased values of λ_T for all previously considered scenarios [17].

Numerous prior studies have considered the phenomenon of drop impingement [18–21]. Drop impact speed affects the impingement dynamics and is often characterized by the Weber number, $We = \rho V^2 D/\sigma$, where ρ is the liquid density, V is the drop impact speed, D is the drop diameter, and σ is the liquid surface tension. Velocity is non-dimensionalized in this manner due to the large influence surface tension exerts on the impinging drop dynamics. As We is increased, the maximum spread the drop experiences increases for all HL, SmH, and SH surfaces [22].

Impingement dynamics have been shown to be greatly altered by the wettability of the surface being impacted [22]. For HL surfaces, an impinging drop will spread until reaching a maximum diameter and then remain deposited on the surface. For impact on SmH surfaces, after reaching its maximum diameter the drop will recoil and may even rebound off of the surface. By making the surface superhydrophobic, the maximum spread diameter and the time before rebound can be altered significantly [22]. The behavior is altered from the SmH surface due to increased contact angle resulting in a larger restoring surface tension force, and increased apparent hydrodynamic slip at the plane of the surface due to the alternating rib and cavity features.

Fig. 3a shows images extracted from high-speed visualization of drops impinging on three surfaces used in this work of varying hydrophobicity at We=85. The temporal progression (time shown along the top of the figure) of each impingement event is shown for HL, SmH, and SH surfaces, where t=0 corresponds to the instant the drop first comes in contact with the surface. Several important points exist in the image sequences. For the HL surface, the drop remains deposited on the surface and does not rebound. In contrast, the drop retracts and rebounds from the SmH and SH surfaces. Also, the progression of the drop spread and retraction differ modestly for the SmH and SH surfaces, with rebound occurring quicker for the SH surface. This behavior is a result of the higher contact angle and lower frictional resistance that prevail on the SH surface. The total contact time before a drop rebounds from a surface is largely independent of We, but scales with $\sqrt{\rho D^3/\sigma}$ [20].

Due to the prevalence of impinging drops in heating or cooling scenarios, the thermal transport from a surface to impinging drops is also of importance [23–25]. When a drop impacts a heated surface, the temperature difference between the drop and the surface and the stagnating behavior of the drop during deformation yields a highly localized heat flux from the surface to the drop [23]. The total amount of heat transferred during the impingement event depends strongly on the impact Weber number [23]. As the drop first comes in contact with the surface, sensible heating of the drop begins and a thermal boundary layer develops that grows over time as the drop spreads [17]. With increasing We the spreading drop attains a larger maximum spread diameter, which increases the interfacial contact area between the surface and the drop [26]. Further, as We increases the drop lamella and the thermal boundary layer decrease, enhancing the heat transfer further.

Not surprisingly, the heat transfer to a drop impinging a SH surface is also a strong function of the SH surface features. Guo et al. considered this problem from both analytical and experimental approaches for

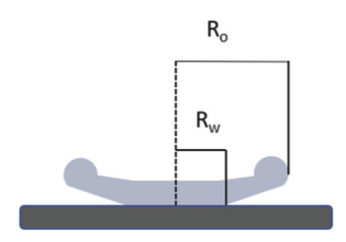


Fig. 4. Diagram illustrating lamella liftoff. Difference between outer and wetted radius is highlighted.

a post structured microscale SH surface [23]. Their model and experimental results showed good qualitative agreement, although the results were limited to small range of Weber numbers $20 \le We \le 40$ and for subcritical surface temperatures only. Their results show that as the solid fraction of the surface decreases, the heat transfer also decreases. They report a 35% reduction in total heat transfer for a SH surface with a F_s of 0.15, compared to the smooth surface scenario ($F_s = 1.0$). Their analytical model predicted an even a larger reduction. It should be noted that in their experiments the SH pitch (center-to-center post spacing) was not varied.

When drops impinge on surfaces heated above the saturation temperature, boiling may occur, depending on how much the surface temperature exceeds the saturation value. At low excess surface temperatures, nucleate boiling prevails where small bubbles are created, enhancing convective heat transfer to the drop. In this regime, the heat flux to the drop increases with increasing surface temperature until the critical heat flux condition is reached. Then the drop enters the transition boiling regime where vapor bubbles grow and coalesce and a vapor film begins to form. Further increasing excess surface temperature, the heat flux decreases until the Leidenfrost Point (LFP) is reached [27]. The above described behavior is consistent with a typical boiling curve, although here the LFP is a function of the impact We [28].

During the nucleate and transition boiling regimes, thermal atomization will occur [29]. Thermal atomization refers to the phenomenon of vigorous vapor bubble formation and subsequent collapse that results in the ejection of many small liquid droplets which depart the primary drop with high speed. At the interface of the impinging drop and the superheated surface, vapor is generated. On a SmH surface this vapor will rise through the impinging drop lamella and burst near its surface, producing the ejection of many microjets that form into satellite droplets. It has been shown that the atomization intensity varies with time after impact, impact speed, and surface temperature; several investigators have defined regime maps that predict the conditions for which thermal atomization will occur [29-32]. These studies have shown that with increasing We the amount of thermal atomization increases, although the excess surface temperature also exerts a strong affect. The atomization intensity is representative of the magnitude of the transient heat transfer to the drop.

During the impingement process on a superheated surface an important phenomenon known as lamella liftoff may occur. It has been shown that at approximately the time when the thermal boundary layer reaches the free surface of the spreading drop, intense evaporation of the drop begins to occur causing the outer edge of the lamella to liftoff from the surface [33]. This liftoff allows vapor that is generated to escape from beneath the drop and consequently the amount of atomization decreases. This liftoff first occurs near the edge of the drop and then the behavior propagates radially inward and the portion of the drop that remains in contact with the surface is known as the wetted radius. The wetted radius, R_w , can be much smaller than the outer radius, R_o , of the spreading drop. Fig. 4 illustrates schematically lamella liftoff and the difference between the outer and wetted radii of the impinging drop. This lamella liftoff behavior significantly reduces the time an impinging drop is in contact with the surface during the impingement event [33]. It should be noted that no prior research has characterized

the lamella liftoff time for SH surfaces and this will be done in this present study.

The wettability of a surface has also been shown to significantly impact the likelihood and intensity of thermal atomization. Clavijo et al. generated a regime map showing that increased superhydrophobicity significantly narrows the range of impact We and surface temperatures where atomization occurs [34]. Fig. 3b shows still images of drops impinging onto superheated HL, SmH, and SH surfaces at several times during the spreading phase of the impingement process. Here, We=85 and the surface, or wall, temperature, T_w , was held constant at 220 °C. The images show that surface wettability significantly affects the overall amount of atomization. Here, maximum atomization occurs on the smooth hydrophobic surface, with a notable reduction in atomization for the other two surfaces. In this study only one SH surface was considered.

Cossali et al. showed that for impingement on SmH surfaces, increasing the roughness of the surface, in general, greatly increases the size of ejected droplets [35]. Atomization has also previously been shown to be a strong function of the surface feature size (w and F_s) [36,27]. Clavijo et al. experimentally explored atomization and how it is altered for a SmH and three different post microstructured SH surfaces [36]. They held the We constant at 85 and quantified the surface temperature where atomization would occur for each SH geometry considered, in addition to quantifying the time varying atomization intensity. They showed that for increasing post center-to-center pitch that atomization intensity decreased. Emerson et al. extended the work of Clavijo and considered impingement over a range of We from 20 to 200 for the same SH surface characteristics [27]. For each surface they identified the conditions of We and T_w where atomization existed. They also determined the temperatures at which maximum atomization was observed as well as the Leidenfrost temperatures for each surface considered. They also postulated that less atomization occurs as the post pitch increases due to the correspondingly larger flow paths for vapor to escape beneath the spreading drop.

While some literature exists on atomization during drop impingement, data for atomization on SH surfaces is still quite limited. This paper will extend the studies of Clavijo and Emerson to explore in great detail how pitch, w, and solid fraction, F_s , affects atomization intensity. First, experiments are conducted for 11 different microscale post patterned SH surfaces. Each of these have different surface characteristics than those considered by Clavijo et al. and Emerson et al. and the results from these experiments show generalized dependence of atomization intensity on a temperature jump length. As will be shown in the next section, the temperature jump length combines the influence of pitch and solid fraction into a single variable. In addition, the lamella liftoff time will be determined for all post structured surfaces and represent the first measurements of this parameter for drop impingement on SH surfaces. Second, experiments are conducted for six microscale rib patterned SH surfaces, providing the first experimental data for atomization on these types of surfaces. Finally, experiments are conducted for SH surfaces comprised of nanoscale features. Here the features are carbon nanotubes (CNTs) that are grown on silicon surfaces.

The remainder of this paper is organized as follows. First, the methods used to conduct the experiments will be described. Then, results showing the temporally varying atomization intensity as a function of temperature will be presented for both post and rib structured SH surfaces. These results will then be used to present a generalized collapse of the data that reveals how atomization depends on the SH surface feature dimensions. Results will then be presented that show atomization is completely suppressed on all nanoscale SH surfaces considered and a hypothesis for why this happens will be presented. Following the results section, conclusions for this work will be given.

Table 1 Dimensions of all post patterned SH surfaces used in this study. The fourth column indicates if atomization was observed on the surface; A = 1 (yes), A = 0 (no).

() //		- / -	
w (µm)	F_s	λ_T (μ m)	A
8	0.26	1.8	1
8	0.1	3.5	1
8	0.06	4.8	1
10	0.08	5.1	1
12	0.16	3.9	1
16	0.44	2.4	1
16	0.38	2.7	1
16	0.25	3.8	1
16	0.1	7	1
24	0.42	3.7	1
24	0.05	15.1	1

Table 2 Dimensions of all rib patterned SH surfaces used in this study. The fourth column indicates if atomization was observed on the surface; A = 1 (yes), A = 0 (no).

w (µm)	F_s	λ_T (μ m)	A
16	0.3	5.2	1
40	0.5	6.4	1
40	0.2	22.0	0
40	0.18	23.3	0
40	0.1	28.1	0
60	0.5	9.6	0

2. Methodology

This section outlines the fabrication process for the SH surfaces, the experimental apparatus and approach, and the high-speed image processing techniques. It also provides equations from which temperature jump length (λ_T) and liquid-surface contact temperature (T_c) are calculated.

2.1. Surface fabrication

All surfaces considered here were made using silicon wafers. For the microscale structured surfaces, microscale arrays of posts or ribs were etched into silicon. Then a thin layer of chromium ($\sim 100~\text{nm}$ thick) was deposited on the silicon surface to facilitate adhesion of the hydrophobic Teflon® coating. Teflon® was applied by a spin coating process which yields a nominal thickness of 200 nm. The thickness of the silicon wafers is 525 μm and the combined thickness of the chromium, and Teflon coating is nominally 0.1% of the thickness of the wafer. Further, the height of the superhydrophobic features on the surface is generally more than 20 times larger than the combined thickness of the combined chromium/Teflon layers. Consequently, thermal resistance caused by the Teflon/chromium is negligibly small compared to the resistance caused by the SH features themselves.

Using this method, contact angles of $\theta \geq 150^\circ$ were obtained for all SH surfaces considered. Smooth hydrophobic surfaces were made by excluding the etching step and for these surfaces $\theta \approx 120^\circ$. A wide range of SH surface geometries were considered for this study. Table 1 provides the dimensions for surfaces with microscale posts and Table 2 gives the same information for all rib structured surfaces. The fourth column in each table is a binary indicator. If the value is 0 then atomization was not observed on this surface for any surface temperature, whereas if the value is 1 then atomization was observed for at least one impact condition. The heights of the SH features varied from 4-15 μ m, however, height was not deemed to be a first order influencer as none of the surfaces met the criteria for drop impalement as proposed by Reyssat et al. [37]. The center-to-center pitch distance, w, and F_s were measured

using a 3D profilometer and the values reported in the table were consistent across the surface to within $\pm 5\%$.

Using the measured values of w and F_s , a temperature jump length, λ_T , was calculated for all post structured surfaces using Eq. (1) from Cowley et al. [15] and these values are also shown in Table 1.

$$\lambda_T = w \left(\frac{0.1756}{\sqrt{F_s}} - 0.1156 \right) \tag{1}$$

The equation above corresponds to steady laminar flow in a parallel plate channel with SH walls with post features and it is derived from a numerical study of the scenario over a very wide range of post and channel sizes. It should be noted that there has not been any prior experimental works that have reported measured values of the temperature jump length for any flow scenario and it is possible that the temperature jump length for an impingement scenario could differ from the scenario of shear flow through a parallel plate channel. However, it is expected that the dependence of λ_T on w and F_s should be similar.

 λ_T was also calculated for all rib structured surfaces considered in the study. It has been shown that the temperature jump length is a function of how the ribs are oriented relative to the flow direction [13,14]. Maynes and coworkers presented values for λ_T for both transverse and streamwise (relative to the flow) oriented ribs for a steady fully-developed parallel plate channel flow [13,14]. For the streamwise orientation it can be determined from the following expression.

$$\lambda_T = (w/\pi) ln(F_c \pi/2) \tag{2}$$

where F_c is the cavity fraction ($F_c = 1 - F_s$). For the transverse rib scenario a simple results were presented graphically and the reader is referred to [14] for the corresponding values. Because fluid is flowing in both transverse and streamwise directions during the impingement event, an average value of λ_T was computed for each surface by using the expressions found in these prior studies. These averaged values of λ_T are included in Table 2.

Nanostructured SH surfaces were also fabricated using silicon wafers. First, layers of alumina and iron, 50 µm and 7 µm thick respectively, were deposited on the silicon to facilitate carbon nanotube growth. Wafers were then diced, placed in a furnace at a temperature of 750 °C, and exposed to hydrogen and methane gas for extended periods of time to allow CNT growth. Growth time of one minute was used for all CNT surfaces resulting in CNT heights of nominally 60 µm. Subsequent nanotube strengthening was performed by increasing the furnace temperature to 900 °C while continuing to flow the hydrogen and methane gasses. This process is known as infiltration and is done to increase CNT diameters by coating the multi-walled CNTs with amorphous carbon. Infiltration time varied from 1-5 minutes, which resulted in CNT diameters varying from 30-75 nm. To yield the surfaces superhydrophobic, the CNT structured surfaces were placed in a vacuum oven and were then baked at 350 °C for 12 hours at a pressure of 17 kPa. This process has been shown to yield high levels of hydrophobicity [10-12].

2.2. Experimental setup

Prior work has shown that the amount of atomization is a strong function of both the surface temperature and We, with atomization increasing as We increases [27]. At low We the atomization intensity is very small or non-existent. At values of $We \geq 120$, peripheral splashing of the drop can occur during the spreading phase. This splashing can occur simultaneously with atomization. To avoid the complexities associated with delineating the difference between droplets formed by splashing versus those formed by the atomization process, all experiments were conducted at a fixed value of We = 85. At this value of We there is significant atomization but splashing is non-existent. The target surface temperature was varied in 20 °C increments from 120 °C up to a maximum of 320 °C. Teflon® begins to degrade at temperatures

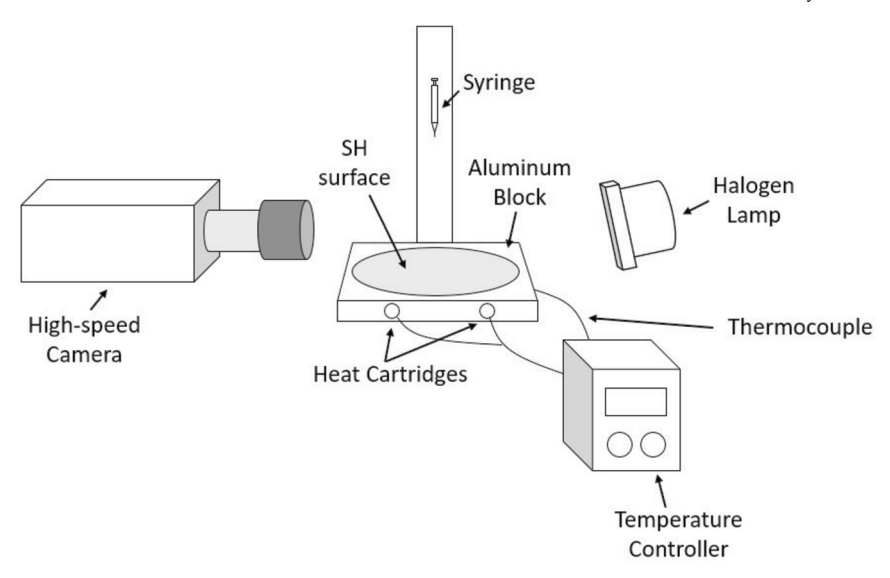


Fig. 5. Schematic of the experimental setup showing positions of the high speed camera, dropper syringe, heated aluminum block, thermocouple and temperature controller, and halogen lamp. The test surface of interest is shown placed on top of the aluminum block.

higher than 340 °C and this limited the upper temperatures that could be explored. The water drop temperature was held constant at nominally 25 °C for all experiments.

Fig. 5 shows a schematic of the experimental setup, lighting, and high-speed camera position. Spherical drops of nearly equal size (D =2.2 mm) were dispensed from a syringe placed at a height that would yield the desired impact condition of We = 85. The test surfaces were mounted on an aluminum block that was heated using embedded heat cartridges. The surface temperature of the aluminum was measured using k-type thermocouples that were located near the center of the aluminum block and immediately below the impingement location on the test surface. A Love Controls Series 2500 temperature controller was used to maintain constant surface temperature of the surface. A Photron APX RS Fastcam Imager was operated at a frame rate of 3000 fps to visualize the time varying behavior during the impingement event. Ten impingement events were captured and the results were averaged to yield a robust measure of the temporal atomization for each surface temperature considered for all surfaces. The test surface was illuminated by a halogen lamp to avoid variations in lighting that exist with AC light sources. The halogen lamp was filled with treated glass to provide diffuse lighting and an evenly illuminated background.

2.3. Image processing

High speed images were analyzed in MATLAB using the same technique used by Clavijo et al. and Emerson et al. [36,27] and are described briefly here. Time varying high-speed images of the dynamical sequence were saved as grayscale images. Each series of images contains an image before the drop enters the frame, referred to as the background image. The sequence then contains all successive images up to the point when the drop has rebounded from the surface. For each analyzed frame, the image is cropped to leave only the impinging drop in the center of the frame. Then the background is subtracted from the original image to eliminate any spurious surface reflections.

Atomization intensity is quantified in each image to be the sum of all pixel values that contain atomized droplets. Some atomized drops are larger or more in focus than others and they have corresponding larger pixel values in the summation. This summation results in a total measure of atomization, A, for that frame. The atomization is thus computed for every frame of the sequence of images to yield atomization data as a function of time. The total atomization is then normalized as $A^* = A/A_{max}$, where A_{max} is the maximum value of atomization that was observed on the SmH surface over the entire range of tempera-

tures explored. This normalization convention is consistent with that used by Clavijo et al. and Emerson et al. [36,27]. It should be noted here that the atomization parameter *A* that is presented is a measure of the area of the atomized drops and not of the volume of the drops. Due to the three-dimensional nature of the atomization event obtaining a volumetric measurement of the atomization is exceeding difficult and would require multiple high-speed synchronized cameras imaging the atomization events from different angles.

To determine the time at which the lamella lifts off of the surface, the instantaneous wetted and outer diameters of the drop were calculated. Fig. 4 illustrates the difference between these two diameters. Similar to the image processing for the atomization measurements, a background image is first subtracted from the original images to eliminate noise. At the time of first drop impact, the surface contact location is identified. After impact, and while the drop is spreading, the distance across the drop is measured at the widest point and this is considered to be the outer diameter. The distance across the bottom of the drop where it is in contact with the surface is also determined from the images and this corresponds to the wetted diameter. Tracking these diameters is followed for every frame throughout the entire impingement event. At some time, these values of R_o and R_w will rapidly begin to deviate as the lamella begins to liftoff from the surface. The time corresponding to the frame where this deviation begins is considered to be the time of lamella liftoff, t_L .

2.4. Contact temperature

As noted above, the surface temperature is measured by thermocouples embedded in the aluminum block. However, the heat transfer from the surface to the drop is dependent on the instantaneous interface temperature. Thus a contact temperature, T_c , is also computed similar to how the interface between two contacting semi-infinite media is computed [17].

$$T_c = \frac{\epsilon_f T_f + \epsilon_w T_w}{\epsilon_f + \epsilon_w} \tag{3}$$

In the above expression, ϵ_f is the effusivity of the fluid, $\epsilon_f = \sqrt{k_f \epsilon_{p,f} \rho_f}$, where k_f is the fluid thermal conductivity, $\epsilon_{p,f}$ is the fluid specific heat, and ρ_f is the fluid density. Substituting in values of the thermophysical properties of fluid from Table 3 yields $\epsilon_f = 1.6 \times 10^3$ J/(m²Ks¹/²). T_f and T_w are the initial temperatures of the fluid drop and wall respectively. The effective effusivity of the wall, ϵ_w , accounts for the effusivity of the silicon as well as the air pockets beneath the

Table 3Thermophysical properties of materials. Parenthetical letters represent the subscript used in nomenclature. CNT properties are used

resent the subscript used in nomenclature. CNT properties are used from Yadav and Sahoo and all other properties are used from Guo et al. [38,23].

Properties	Water (f)	Silicon (s)	Air (a)	CNT (CNT)
ρ (kg/m ³)	998	2329	1.29	852
ρ (kg/m ³) c_p (J/kg-K) k (W/m-K)	4200	700	1006	1800
k (W/m-K)	0.6	120	0.026	0.15

drop as outlined by Guo et al. [23]. Based on the solid fraction of the SH surface, this effusivity is calculated as $\epsilon_w = \epsilon_s F_s + \epsilon_a (1-F_s)$, where ϵ_s and ϵ_a are the effusivity of silicon and air, respectively. This effusivity assumes no penetration of water in the cavities. Using the respective thermophysical properties of silicon and air from Table 3 yields $\epsilon_s = 1.4 \times 10^4$ and $\epsilon_a = 5.8$ J/(m²Ks¹/²).

The contact temperature will be used in later analysis regarding atomization onset temperature and suppression of atomization on nanoscale structures.

3. Results and discussion

Results from this study are organized as follows. First, atomization data will be presented for impingement on microscale structured surfaces. The time varying atomization as a function of surface temperature is presented for both post and rib structured surfaces at several surface temperatures. For every transient scenario a maximum in the atomization intensity exists. This maximum value is identified for each case and then this value will be shown as a function of the surface temperature for all microstructured surfaces. Further, the time when this maximum value occurs is also identified and this time will be compared to the measured lamella lift-off time. Then impingement behavior on CNT surfaces will be discussed. Temporally varying atomization data is not presented for CNT surfaces since atomization was never observed for any condition explored. A hypothesis for why atomization is completely suppressed on all CNT structures will then be provided. Finally, generalized behavior of all surfaces will be presented in terms of a temperature jump length.

3.1. Atomization of microstructured surfaces

Fig. 6 shows A^* as a function of time on the SmH surface and five different SH surfaces. Fig. 6a provides A^* vs time data at four different surface temperatures (180, 200, 220, and 280 °C) for the SmH surface as a benchmark against which to compare results for each of the SH surfaces. Panels b-f provide results for the five SH surfaces and for each, corresponding values of w, F_s , and λ_T are listed. Recall that the impingement We is 85 for all results and t=0 corresponds to the instant the drop first comes in contact with the surface. For each SH surface results are shown over a range of surface temperatures that encompass the conditions where atomization was observed for each respective surface. Experiments were conducted over a wider range of surface temperatures than shown in the figures. However, data are not shown for all scenarios considered to increase clarity of observed trends.

The horizontal and vertical axes are the same for all panels of Fig. 6 to allow comparison between the various cases. However, for the surfaces with low levels of atomization (Fig. 6b, e, and f) inset plots are also included to better illustrate the smaller atomization values that exist on these surfaces. Panel b provides data for one of the two rib structured surfaces that exhibited appreciable atomization while panels c-f show results for four post-structured surfaces and depict important trends for variations in F_s and w. When the post center-to-center pitch is held constant while F_s decreases from 0.25 to 0.1 the time varying atomization curve is lowered significantly. This is shown by comparing results shown in panels c and d where the pitch is held constant at 8 μ m, and

in panels e and f where the pitch is held constant at 16 um. The maximum observed atomization in panel c ($w = 8 \mu m$ and $F_s = 0.26$) is approximately five times greater than that shown in panel d ($w = 8 \mu m$ and $F_s = 0.1$). Similarly, the maximum observed atomization in panel e ($w = 16 \mu m$ and $F_s = 0.25$) is approximately 80 times greater than that shown in panel f (w = 16 μ m and Fs = 0.1). Further, when F_s is held constant, at either 0.25 or 0.1, then as w increases from 8 μ m to 16 µm atomization intensity is again significantly decreased by similar magnitudes. This reduction is shown by comparing results shown in panels c and e where the solid fractions are 0.25 and 0.26, and in panels d and f where the solid fraction is held constant at 0.1. Note that A^* curves with the largest magnitude shown in Figs. 6d and 6e are similar in magnitude, despite the surfaces having very different values of F_s and w. The temperature jump lengths (as calculated using Eq. (1)) for these two surfaces, however, are similar. This suggests that λ_T is a more important parameter for understanding the thermal transport to impinging drops than either F_s or w alone. Note that data for only two temperatures (240 °C and 280 °C) are shown in Fig. 6d. At surface temperatures lower than 240 °C and greater than 280 °C no atomization was observed. At 260 °C the atomization curve was nearly identical to the 280 °C case and for clarity these data are not shown.

For all cases shown in all panels of Fig. 6, $A^*=0$ at t=0 and then increases as the number of ejected droplets increases. These ejected droplets have significant velocity and shortly after atomization ceases to be produced, some of the small atomized droplets begin to leave the field of view, resulting in a decrease in A^* as time continues to increase. Thus, a maximum in the A^* vs t data exists for all cases and this peak is denoted as A_m^* . The time at which this maximum atomization amount occurs is referred to in this paper as t_m and both A_m^* and t_m vary for surfaces of different surface microstructure. In this study t_m was observed to vary from 2.66 ms to 4.33 ms.

The data show that A_m^* is a strong function of surface temperature. As surface temperature increases, A_m^* initially increases until a maximum is reached and A_m^* then decreases until zero atomization is observed. The temperature corresponding to the largest value of A_m^* also depends strongly on the surface microstructure and this value is denoted as T_m . For example, for the $F_s=0.26$ and w=8 µm surface, the largest A_m^* is achieved at a $T_w=280\,^{\circ}\mathrm{C}$ while for the $F_s=0.1$ and w=16 µm surface A_m^* occurs at a much lower surface temperature (160 °C). The value of T_m is shown later to depend systematically on λ_T .

The peak in atomization intensity, A_m^* , may occur due to either a decrease in heat transfer to the drop, or to an alternative path of vapor to escape from beneath the drop. When the lamella begins to liftoff of the surface, the wetted area between the drop and the surface decreases reducing the corresponding heat transfer to the drop. Also, as the lamella begins to liftoff, some vapor formed near the surface and outer edges of the drop is able to escape from beneath the drop. This suggests that there is correspondence between the time when the atomization is at a maximum and when the lamella lifts off. Fig. 7 shows the measured values of t_m as a function of the measured values of t_I . The lamella liftoff is determined, as explained in the preceding section, to be the time when the measured outer radius of the drop departs from and exceeds the wetted radius. Each data point shown in Fig. 7 represents the scenarios shown for the SmH and three post patterned SH surfaces where significant atomization was prevalent. These surfaces are those listed in the legend of Fig. 8a. It should be noted that these surfaces were selected as lamella liftoff is difficult to measure on surfaces with low atomization and is even non-existent when atomization magnitudes are sufficiently low. Note the discrete nature of t_m and t_L data, this is due to the frame rate of the camera which captures an image every 0.333 ms. For this reason error bars have been added in both the x and y directions. An equivalence line is included on the figure to emphasize that the measured value of t_m and t_L support the hypothesis that these events occur nearly simultaneously.

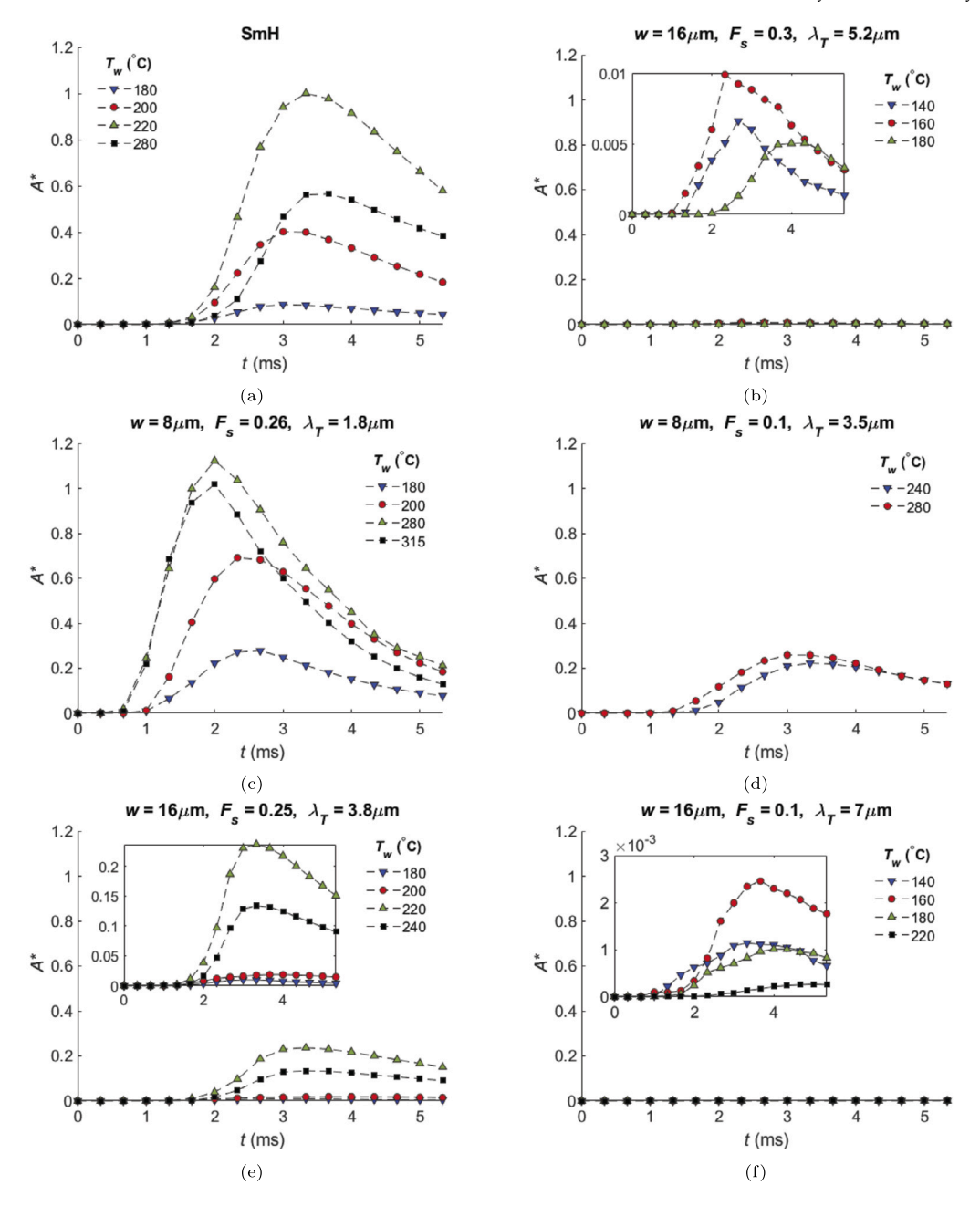


Fig. 6. A^* vs t for various surfaces at We = 85 for all results: a) SmH surface; b) Ribbed SH surface; (c-f) Four post patterned SH surfaces of varying geometry. Surface dimensions and λ_T are provided at the top of each panel and results are shown for each case at multiple wall temperatures.

We now consider how A_m^* varies with surface temperature and surface properties. Fig. 8 presents A_m^* as a function of surface temperature, T_w . Three panels of data are shown that include surfaces where relatively large (panel a), medium (panel b), and small (panel c) amounts of atomization were observed. Notice that the three panels have different vertical axes corresponding to the varying magnitudes of $A_{...}^*$. Experiments were performed on all of the surfaces shown in Table 1, however, the results shown are reduced in order to maintain clarity. It should be noted here that atomization was not observed on any surface where the temperature jump length was greater than 6 µm (with the exception of one post patterned surface) and this includes all but two of the rib patterned surfaces, as shown in Table 2. The post patterned surface that behaves unexpectedly is thought to have experienced partial wetting due to its relatively small solid fraction and large pitch (F_s = 0.05 and $w = 24 \mu m$). Filled and open data markers correspond to post and rib structured surfaces respectively.

The data in Fig. 8 show that A_m^* increases with increasing wall temperature until it reaches a maximum at a surface temperature defined to be T_m . As the wall temperature is increased beyond this value, transition boiling behavior prevails, and atomization intensity decreases until the LFP is reached. The data of Fig. 8 show that A_m^* exhibits a strong dependence on the SH surface solid fraction and pitch values. It was noted above that when w is held constant, A_m^* decreases with a decrease in F_s and, for constant F_s , A_m^* decreases with increasing w. The data also show that the overall maximum amount of atomization that was observed does not occur on the SmH surface. Instead, values of A_m^* for the $F_s = 0.26$ and $w = 8 \mu m$ and for the $F_s = 0.44$ and $w = 16 \mu m$ surfaces exceed the smooth surface values. As noted in the introduction, when microstructures are added to a surface and the Cassie state prevails, the amount of heat transfer can be reduced notably. However, adding microstructures also increases the number of bubble nucleation sites that exist on the surface, which would yield an increase in the rate of bub-

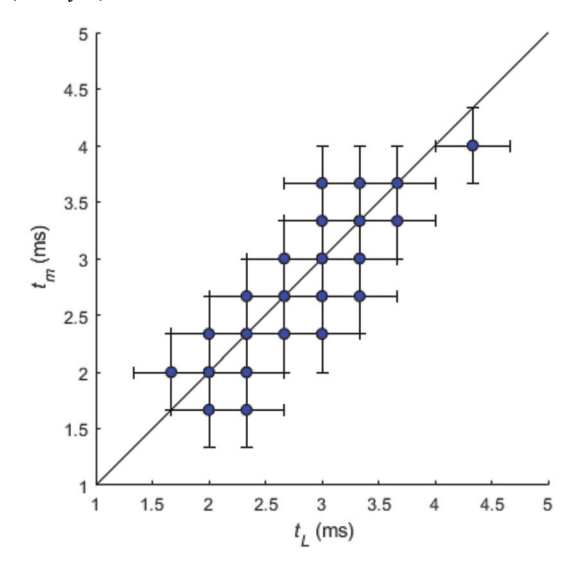


Fig. 7. Time when the maximum atomization is observed, t_m , as a function of the lamella liftoff time, t_r .

ble formation/collapse. Thus, the process of placing microstructure on a surface yields competing affects when boiling occurs. It is hypothesized that for the $F_s=0.26$ and $w=8~\mu m$ and $F_s=0.44$ and $w=16~\mu m$ surfaces that the combination of relatively large solid fractions and small pitch values yield an increased density of nucleation sites that results in an increase in bubble formation and the corresponding increase in observed atomization. Then, as the solid fraction decreases or as the pitch increases, the reduction in heat transfer exercises greater influence and the amount of boiling and atomization decreases.

The data of Fig. 8 also show that the value of T_w where atomization begins, the value of T_w when atomization is a maximum (T_m) , and the value of T_w when the LFP is reached are all functions of F_s and w. T_m is analogous to the temperature at the critical heat flux when considering the classical boiling curve. The value of T_m extracted from the A_m^* vs T_w curves does not maintain a consistent trend based on either F_s or w alone. The Leidenfrost temperature, T_{LF} , while more difficult to quantify than T_m due to experimental temperature limitations, also varies with F_s and w. Later in the paper it will be shown that T_m and T_{LF} are very well correlated by using the concept of the temperature jump length and how these vary with λ_T will be presented.

3.2. Atomization on CNT SH surfaces

As stated above, atomization was not observed during impingement on any superheated CNT surfaces regardless of the magnitude of the surface temperature. Two types of CNT structures were explored, CNT structures coating a micro-structured surface (two-tiered surface), and a uniform distribution of CNTs that were grown on a smooth surface. The two-tiered surface had CNTs that were grown on a post structured surface with $F_s = 0.2$ and w = 12. For all CNT surfaces, the CNTs were grown for one minute and this yielded uniform heights of nominally 60 μm. The microscale post structures maintained their shape after the CNTs were grown at equal rates on top of the posts and inside of the cavities. Five two-tiered and five smooth surfaces were fabricated and tested. The infiltration time was varied in one minute intervals from 1-5 minutes. Recall that infiltration results in increased diameter of the CNT's, but doesn't change their height. After infiltration, the diameters of the CNTs ranged between 30-75 nm. Regardless of CNT diameter or surface type (two-tiered or smooth), impingement events consistently yielded zero atomization. This prevented drawing conclusions regarding impact of CNT size on atomization intensity.

The suppression of all atomization on the CNT coated surfaces is attributed to the low effusivity of the CNTs. Physical properties of CNTs

are variable and difficult to quantify. Here values are used from Yaday and Sahoo for the CNT thermal conductivity (k_{CNT}), specific heat $(c_{p,CNT})$, and density (ρ_{CNT}) which are recorded in Table 3 [38]. Solid fraction is not able to be quantified for CNTs, but for the upper limit case ($F_s = 1.0$) the thermophysical property values yield $\epsilon_{CNT} = 4.79$ \times 10² J/(m²Ks^{1/2}). By comparison, the effusivity of silicon is nominally 30 times higher ($\epsilon_s = 1.40 \times 10^4 \text{ J/(m}^2\text{Ks}^{1/2})$). The implication of the very low effusivity is more clear when the contact temperature is calculated following the approach outlined in section 2.4, where T_c is calculated to be significantly lower for drops impinging onto a CNT surface. In effect, the low effusivity of the CNTs combined with the trapped air between them yields a very large thermal resistance that results in the contact temperature always being lower than the saturation temperature. Shown in Fig. 9 are values of T_c , calculated using Eq. (3), as a function of T_w . Computed values are shown for three micro-structured silicon surfaces with varying F_s (0.1, 0.25, and 0.5). As T_w increases, T_c increases linearly for all cases. When T_c is less than T_{sat} (100 °C), phase change should not occur. Thus, for the silicon surfaces, the temperature where boiling would first be observed moves from approximately 120 °C for the $F_s = 0.5$ surface to 135 °C for the $F_s = 0.25$ surface and finally to 185 °C for the $F_s = 0.1$ surface. Values are also shown for a CNT coated surface. Even if we assume $F_s = 1.0$ (thought the actual F_s will be much smaller), the contact temperature never exceeds T_{sat} over the range of wall temperatures considered in this study. This suggests that atomization should indeed never be observed for impingement on CNT surfaces over the range of surface temperatures considered. In reality, the contact temperature on a CNT surface will be even lower than that shown in Fig. 9 because here the limiting case of $F_s = 1.0$ is considered. The T_c values shown in the figure also suggest that the onset of boiling and atomization on silicon SH surfaces should occur at different temperatures, depending on the F_s of the surface. Values of T_w at which atomization begins to occur differ greatly in Fig. 8. However, values of T_c at which atomization begins to occur are clustered much more tightly and most surfaces display atomization at a T_c close to the saturation point.

3.3. Generalized atomization parameters

It was observed that increasing F_s and w exert competing influences on the intensity of atomization. Here the critical parameters of A_m^* , T_m , and t_m are considered and presented in terms of the calculated temperature jump length, λ_T . The contact temperature concept is also used to further explore generalized behavior.

Shown in Fig. 10 is the maximum value of A_m^* that was observed for every surface considered in the study where atomization was observed. This value is presented as a function of the computed value of λ_T that is included in Tables 1 and 2. The surface temperature for each data point corresponds to the unique value of T_m that exists for each respective surface. Thus, the data shown correspond to different surface temperatures. Recall that the values of λ_T show in Tables 1 and 2, and that form the horizontal axis of Fig. 10, correspond to the straightforward steady fully-developed channel flow scenario. We do not believe that these values represent the exact temperature jump length for the complex unsteady spreading and retraction dynamics that exist in the impingement event considered here. In this event it is likely that the temperature jump length itself is not constant, either temporally or spatially. Rather, we use them here to show how important parameters from the current study collapse to single representative curves using these values of λ_T . Indeed, these values do a good job of combining the solid fraction and SH surface center-to-center pitch spacing into a single parameter that provides good correlation of the experimental data. Future work is warranted that explores from a computational point of view how the temperature jump length changes over time and space for the complex dynamical scenario of droplet impingement.

The value of $\lambda_T=0$ corresponds to that for the smooth surface (SmH) and this surface is considered to be the baseline against which

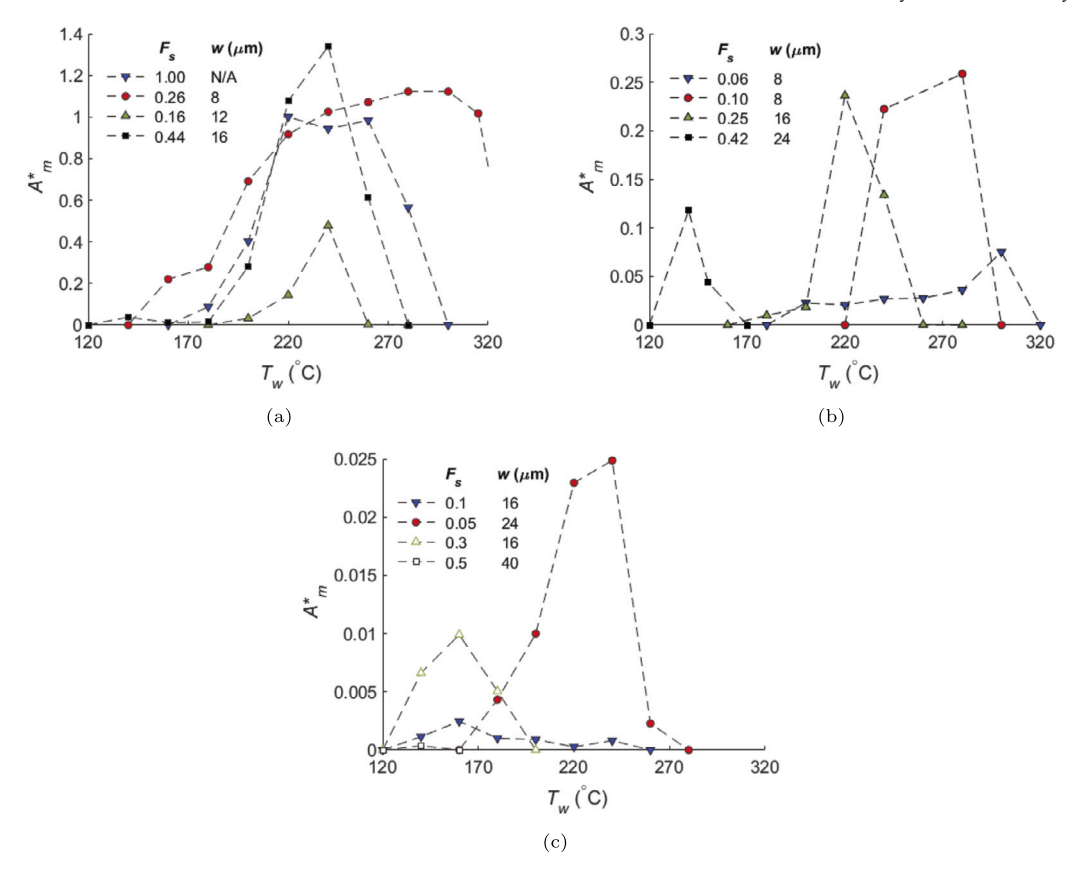


Fig. 8. A_m^* vs T_w for impingement at We = 85 on: (a) the SmH surface and three post structured SH surfaces of varying geometry; (b) four post structured SH surfaces of varying geometry; (c) two post structured SH surfaces (filled markers) and two rib structured SH surfaces (open markers). The vertical axes differ for each panel due to large differences in the atomization magnitudes.

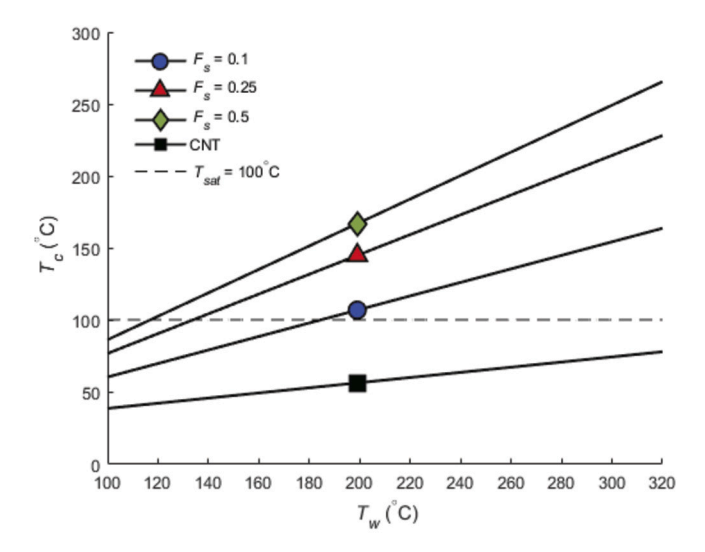


Fig. 9. Contact temperature T_c , as computed from Eq. (3), as a function of surface temperature, T_w . Values for a CNT surface are compared to those of a micro-structured silicon surface of varying F_s .

levels of atomization for all other surfaces are compared. As λ_T is increased above 0 the maximum atomization value actually increases modestly up to $\lambda_T=2.5$. For example, it is nominally 35% higher for the $F_s=0.44$ and w=16 µm surface than for the SmH surface. Again, it is proposed that this increase is due to the structured surfaces having many more nucleation sites than the smooth scenario. Then as λ_T continues to increase above 2.5, the value of A_m^* drops rapidly. In the range of $2.5 \le \lambda_T \le 6$ the value of A_m^* decreases towards zero. For the range

 $\lambda_T > 6$ atomization was observed, but the magnitude was negligibly small. As shown in Tables 1 and 2, atomization was never observed on four microscale surfaces and those surfaces all have λ_T values greater than 6.0.

As illustrated by the data of Fig. 8, a large variation in the value of T_w marking the onset of atomization was observed and this temperature is a strong function of the surface characteristics. For each surface, after data was collected over the entire temperature range, the surface temperature at which maximum atomization occurred was recorded. This temperature was then converted to a contact temperature using Eq. (3) and is denoted as $T_{c,m}$. It is further considered how the corresponding value of $T_{c,m}$ depends on the temperature jump length. Shown in Fig. 11a is the $T_{c,m}$ data as a function of the computed temperature jump length. Presented in this form the data tend to collapse toward a single representative curve and a trend line is included in the figure to illustrate the systematic behavior dependency of $T_{c,m}$ on λ_T . The error bars are indicative of the experiments being conducted in 20 °C increments. Three data points are also included from surfaces considered previously by Clavijo et al. and one data point is included from the study conducted by Emerson et al. [27,36]. These data fall consistently on the trend of the current data.

An important outcome of this work is that the data of Fig. 11a allow a priori prediction of the temperature at which maximum atomization will be observed on a surface as a function of the corresponding value of λ_T for a superhydrophobic surface of interest. Interestingly, the observed atomization on the SmH surface ($\lambda_T=0$) has a maximum at a value of $T_{c,m}$ that is slightly lower than that of the SH surface with the lowest λ_T value explored (the $F_c=0.26$, w=8 µm surface with $\lambda_T=1.8$). As λ_T increases above 1.8, $T_{c,m}$ decreases systematically. For values of $\lambda_T>6.0$ the trend line suggests a value of $T_{c,m}$ that drops below 100 °C. Recall that for these surfaces the amount of atomization (even

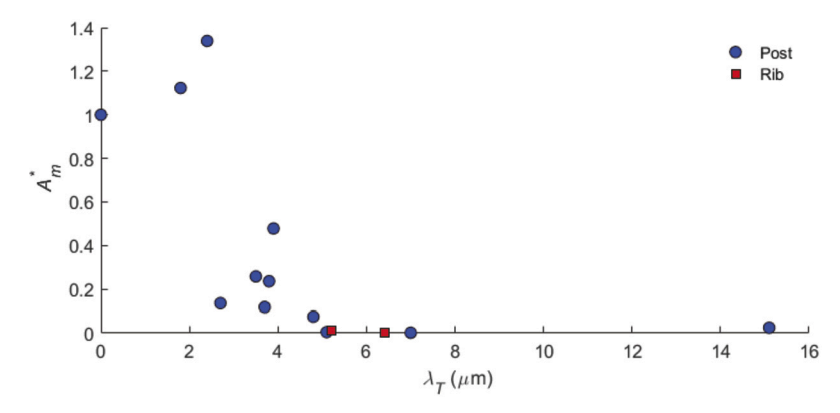


Fig. 10. Maximum normalized atomization, A_m^* , as a function λ_T . For each surface the value of A_m^* is taken at the surface temperature resulting in the largest magnitude of atomization.

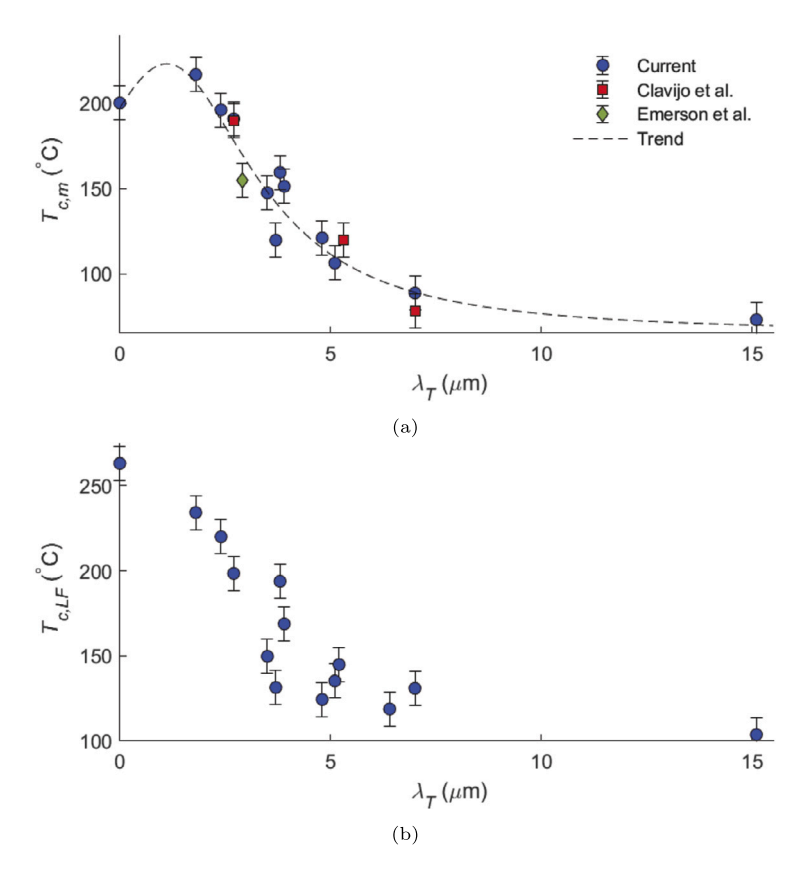


Fig. 11. (a) Contact temperature corresponding to the point maximum atomization, $T_{c,m}$, as a function of λ_T . (b) Contact temperature corresponding to the Leidenfrost point, $T_{c,LF}$, as a function of λ_T . Data from Emerson et al. and Clavijo et al. are included as indicated [27,36].

for the maximum condition) was very small or non-existent. The fact that $T_{c,m}$ drops below the saturation temperature at $\lambda_T > 6.0$ is consistent with the A_m^* data of Fig. 10 that showed minimal atomization for surfaces with $\lambda_T > 6.0$.

Shown in Fig. 11b is the computed value of the contact temperature at the point where Leidenfrost behavior prevails, $T_{c,LF}$, or where all atomization has ceased, as a function of λ_T . $T_{c,LF}$ is again computed from Eq. (3), using the wall temperature where the atomization level has dropped back down to zero. Of course, the value of $T_{c,LF}$ exceeds $T_{c,m}$ for all surfaces but the shape of the trends with varying λ_T are similar. In general, the LFP was more difficult to quantify than the point of maximum atomization. This is because for some scenarios experiments could not be conducted at sufficiently high surface temperature due to limitations in the experimental setup. Regardless the trends in $T_{c,LF}$ and $T_{c,m}$ with λ_T are consistent.

Shown in Fig. 12 are the same values of A_m^* that are shown in Fig. 10, but now plotted as a function of the corresponding contact temperature $T_{c,m}$. Results are shown for all scenarios where the impingement events yielded non-negligible levels of atomization. The data generally reveals a systematic increase in A_m^* as the computed value of $T_{c,m}$ increases providing an alternative way of interpreting the data. Data are only shown for scenarios where measurable atomization existed and the results show clearly that if the contact temperature is lower than approximately 110 °C that significant atomization will never be expected for microscale structured surfaces, even if the surface temperature is very high.

We now turn our attention to how the time of maximum atomization, t_m , varies with λ_T . Fig. 13 provides these data for all surfaces where atomization was observed. Similar to the $T_{c,m}$ data, the corresponding times cluster toward a single representative curve, which is

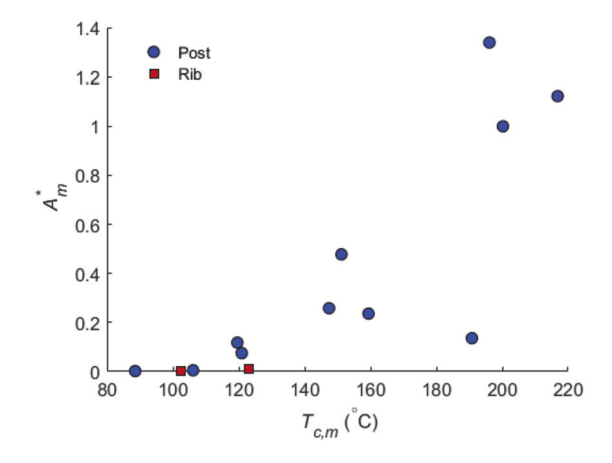


Fig. 12. Maximum atomization vs $T_{c,m}$. Each data point represents the peak A_m^* of a specific surface at the corresponding $T_{c,m}$ at which it was generated. We = 85.

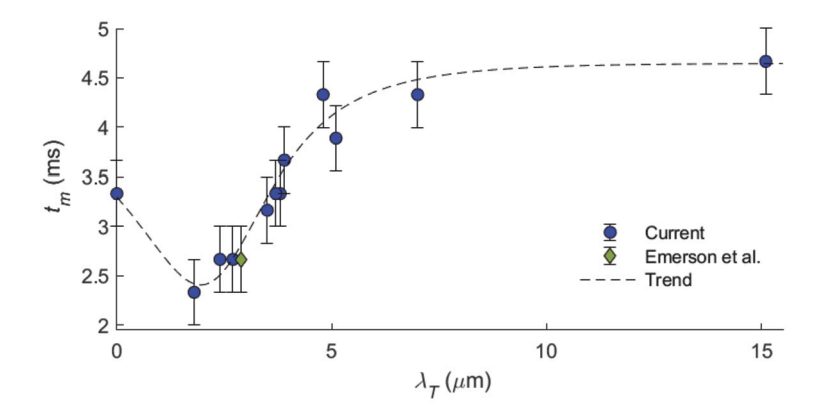


Fig. 13. Time after impact at which the maximum atomization is observed as a function of λ_T . Data is included from Emerson et al. [27].

illustrated with a trend line on the plot. Generally, for the non-zero λ_T values explored in this work, t_m increases with increasing λ_T . Here the SmH surface exhibits a time of nominally 3.2 ms and t_m decreases below this for the first SH surface considered. At larger values of λ_T , t_m then increases with increasing λ_T . The error bars on the data correlate to the frame rate of the high speed imaging, which was 3,000 fps. Data is also included from Emerson et al. and it falls along the trend of all current data [27]. Data of this kind was not available from the study done by Clavijo et al. which was used for previous validation.

To recapitulate, the data of Figs. 10, 11, and 12 reveal that for We=85 atomization would not be expected for any microscale featured SH surfaces when λ_T is greater than 6 μ m when the drop does not wet the surface. Another implication of the data is that at $\lambda_T>6$ μ m, film boiling or Leidenfrost type behavior prevails over the entire range of possible surface temperatures explored here. Further, the systematic variation of $T_{c,m}$, t_m , and A_m^* with λ_T allows first order prediction of how much atomization (a measure of the amount of phase change) would be occurring as a function of the SH surface characteristics. This information would be valuable in developing predictive models of the rate of drop vaporization during impingement process on hot SH surfaces.

4. Conclusions

Thermal atomization intensity of a liquid drop impinging on superheated surfaces was investigated at an impact Weber number of 85. A SmH surface and several SH surfaces with micro-structured and nano-structured geometry were considered. Micro-structured geometry consisted of post and rib patterned micro-arrays defined by their pitch and solid fraction. Nano-structured geometry consisted of CNT structures of varying nanotube diameter.

For a single impingement event, atomization increases with time until peaking at the point of lamella liftoff. The magnitude of the atomization is dependent on the surface temperature and geometric features of the SH surface and the time when the maximum atomization occurs is dependent on the SH features. During impingement, atomization magnitude increases until peaking where transition boiling begins to occur, it then decreases until the LFP is achieved. The surface temperatures where the atomization reaches a maximum and then the LFP is attained also vary with surface geometry. For all of the results presented here the temperature of the drop was equal to nominally 25 °C It should be noted that as the water drop temperature increases the wall temperature where atomization begins would decrease and the overall magnitude of atomization would increase. Investigating the specific influence of drop temperature on the atomization dynamics is worthy of a future study.

For micro-structured surfaces, pitch and solid fraction may be combined into a single parameter, λ_T and the atomization magnitude has been shown to generally decrease with increasing λ_T . Further, the contact temperature, $T_{c,m}$, and time, t_m , at which maximum atomization occurs were shown to behave systematically with λ_T . The current data allow a priori prediction of the conditions under which atomization will occur for impingement on SH surfaces. The following provide a summary of primary conclusions regarding the microstructured surfaces:

- 1. Atomization was completely suppressed on all surfaces where λ_T is greater than 6 μm .
- 2. Interestingly, the maximum observed atomization occurred for a surface with $\lambda_T=2~\mu m$ and the value was about 30% greater than the maximum observed for a smooth hydrophobic surfaces.

- 3. For all surfaces where $\lambda_T > 6$ µm, film boiling, or Leidenfrost, type behavior prevails over the entire range of surface temperatures that were explored.
- 4. The contact temperature at the Leidenfrost point was nominally 260 °C for the smooth surface and it decreased from to a value of approximately 120 °C for surfaces with $\lambda_T=6~\mu m$.
- 5. The time after impact when maximum atomization occurs was also shown to be a strong function of λ_T . It is reaches a minimum value of 2.5 ms for surfaces with $\lambda_T=2~\mu m$ (decreasing from 3.4 ms for the smooth surface) and then increasing to approximately 4.3 ms for surfaces with $\lambda_T=6~\mu m$.

The focus of the paper was to explore the impact of variations in the SH surface feature dimensions (height, pitch, and cavity fraction) on atomization over the range of surface temperatures where atomization was observed for each surface. A single impact Weber number (85) was chosen to keep the scope of the work reasonable. Previous work by Emerson et al. [27] considered variations in the impact Weber number. They considered Weber number values of 20, 40, 85, 150, and 220, but for only three different post patterned SH surfaces. They observed that the maximum atomization intensity was similar at We = 85, 150, and 220, while it decreased with decreasing We for the lower scenarios. It is thus expected that the conclusions of the current paper will yield similar results at $We \geq 85$, with diminishing atomization as We decreases.

Atomization was completely suppressed on all nanoscale structured (CNT) SH surfaces over the entire range of temperatures explored. This is thought to be due to the low thermal effusivity of the CNTs that were grown on the surface. Due to the effective insulation of the CNT layer, the computed contact temperature never exceeds saturation over the temperature range explored in this work.

Declaration of competing interest

The authors declare that they have no known competing financial interests or personal relationships that could have appeared to influence the work reported in this paper.

Data availability

Data will be made available on request.

Acknowledgements

This material is based upon work funded by the National Science Foundation (grant number CBET-1707123).

References

- [1] M.Z. Khan, J. Militky, M. Petru, B. Tomková, A. Ali, E. Tören, S. Perveen, Recent advances in superhydrophobic surfaces for practical applications: a review, Eur. Polym. J. 178 (2022), https://doi.org/10.1016/j.eurpolymj.2022.111481.
- [2] S. Humayun, R.D. Maynes, J. Crockett, B.D. Iverson, Retention forces for drops on microstructured superhydrophobic surfaces, Langmuir 38 (2022) 15960–15972, https://doi.org/10.1021/acs.langmuir.2c02290.
- [3] W. Ren, Z. Lian, J. Wang, J. Xu, H. Yu, Fabrication of durable underoil superhydrophobic surfaces with self-cleaning and oil-water separation properties, RSC Adv. 12 (2022) 3838–3846, https://doi.org/10.1039/d1ra06422c.
- [4] B. Bhushan, Y.C. Jung, Natural and biomimetic artificial surfaces for superhydrophobicity, self-cleaning, low adhesion, and drag reduction, Prog. Mater. Sci. 56 (2011) 1–108, https://doi.org/10.1016/j.pmatsci.2010.04.003.
- [5] W. Huang, J. Huang, Z. Guo, W. Liu, Icephobic/anti-icing properties of superhydrophobic surfaces, Adv. Colloid Interface Sci. 304 (2022), https://doi.org/10. 1016/j.cis.2022.102658.
- [6] J.M. Beér, High efficiency electric power generation: the environmental role, Prog. Energy Combust. Sci. 33 (2007) 107–134, https://doi.org/10.1016/j.pecs.2006.08. 002.
- [7] D. Attinger, C. Frankiewicz, A.R. Betz, T.M. Schutzius, R. Ganguly, A. Das, C.-J. Kim, C.M. Megaridis, Surface engineering for phase change heat transfer: a review, MRS Energy Sustain. 1 (2014), https://doi.org/10.1557/mre.2014.9.

- [8] A.D. Khawaji, I.K. Kutubkhanah, J.M. Wie, Advances in seawater desalination technologies, Desalination 221 (2008) 47–69, https://doi.org/10.1016/j.desal.2007.01.067
- [9] T. Humplik, J. Lee, S.C. O'Hern, B.A. Fellman, M.A. Baig, S.F. Hassan, M.A. Atieh, F. Rahman, T. Laoui, R. Karnik, E.N. Wang, Nanostructured materials for water desalination, Nanotechnology 22 (2011), https://doi.org/10.1088/0957-4484/22/ 29/292001.
- [10] K.A. Stevens, C.D. Esplin, T.M. Davis, D.J. Butterfield, P.S. Ng, A.E. Bowden, B.D. Jensen, B.D. Iverson, Superhydrophobic, carbon-infiltrated carbon nanotubes on Si and 316L stainless steel with tunable geometry, Appl. Phys. Lett. 112 (2018), https://doi.org/10.1063/1.5034471.
- [11] A.I. Aria, M. Gharib, Reversible tuning of the wettability of carbon nanotube arrays: the effect of ultraviolet/ozone and vacuum pyrolysis treatments, Langmuir 27 (2011) 9005–9011, https://doi.org/10.1021/la201841m.
- [12] A.I. Aria, M. Gharib, Dry oxidation and vacuum annealing treatments for tuning the wetting properties of carbon nanotube arrays, J. Visual. Exp.: JoVE (2013), https://doi.org/10.3791/50378.
- [13] D. Maynes, B.W. Webb, J. Crockett, V. Solovjov, Analysis of laminar slip-flow thermal transport in microchannels with transverse rib and cavity structured superhydrophobic walls at constant heat flux, J. Heat Transf. 135 (2013), https:// doi.org/10.1115/1.4007429.
- [14] D. Maynes, J. Crockett, Apparent temperature jump and thermal transport in channels with streamwise rib and cavity featured superhydrophobic walls at constant heat flux, J. Heat Transf. 136 (2014), https://doi.org/10.1115/1.4025045.
- [15] A. Cowley, D. Maynes, J. Crockett, Inertial effects on thermal transport in superhydrophobic microchannels, Int. J. Heat Mass Transf. 101 (2016) 121–132, https:// doi.org/10.1016/j.ijheatmasstransfer.2016.05.037.
- [16] C.L.M.H. Navier, Memoire sur les lois du mouvement des fluides, Mém. Acad. Sci. Inst. Fr. (1823).
- [17] J.C. Burnett, Thermal transport to impinging droplets on superhydrophobic surfaces, Master's thesis, Brigham Young University, 2021.
- [18] I.V. Roisman, E. Berberović, C. Tropea, Inertia dominated drop collisions. I. On the universal flow in the lamella, Phys. Fluids 21 (2009), https://doi.org/10.1063/1. 3129282.
- [19] I.V. Roisman, Inertia dominated drop collisions. II. An analytical solution of the Navier-Stokes equations for a spreading viscous film, Phys. Fluids 21 (2009), https://doi.org/10.1063/1.3129283.
- [20] Z. Hu, F. Chu, Y. Lin, X. Wu, Contact time of droplet impact on inclined ridged superhydrophobic surfaces, Langmuir 38 (2022) 1540–1549, https://doi.org/10.1021/ acs.langmuir.1c03001.
- [21] P. Attané, F. Girard, V. Morin, An energy balance approach of the dynamics of drop impact on a solid surface, Phys. Fluids 19 (2007), https://doi.org/10.1063/1. 2408405
- [22] C.E. Clavijo, J. Crockett, D. Maynes, Effects of isotropic and anisotropic slip on droplet impingement on a superhydrophobic surface, Phys. Fluids 27 (2015), https://doi.org/10.1063/1.4936899.
- [23] C. Guo, D. Maynes, J. Crockett, D. Zhao, Heat transfer to bouncing droplets on superhydrophobic surfaces, Int. J. Heat Mass Transf. 137 (2019) 857–867, https:// doi.org/10.1016/j.ijheatmasstransfer.2019.03.103.
- [24] G. Castanet, O. Caballina, W. Chaze, R. Collignon, F. Lemoine, The Leidenfrost transition of water droplets impinging onto a superheated surface, Int. J. Heat Mass Transf. 160 (2020) 120–126, https://doi.org/10.1016/j.ijheatmasstransfer. 2020.120126.
- [25] H. Chaves, A.M. Kubitzek, F. Obermeier, Dynamic processes occurring during the spreading of thin liquid films produced by drop impact on hot walls, Int. J. Heat Fluid Flow 20 (1999), https://doi.org/10.1016/S0142-727X(99)00034-X.
- [26] N. Samkhaniani, A. Stroh, M. Holzinger, H. Marschall, B. Frohnapfel, M. Wörner, Bouncing drop impingement on heated hydrophobic surfaces, Int. J. Heat Mass Transf. 180 (2021), https://doi.org/10.1016/j.ijheatmasstransfer.2021.121777.
- [27] P. Emerson, J. Crockett, D. Maynes, Thermal atomization during droplet impingement on superhydrophobic surfaces: influence of Weber number and micropost array configuration, Int. J. Heat Mass Transf. 164 (2021), https://doi.org/10.1016/j.ijheatmasstransfer.2020.120559.
- [28] M. Searle, P. Emerson, J. Crockett, D. Maynes, Influence of microstructure geometry on pool boiling at superhydrophobic surfaces, Int. J. Heat Mass Transf. 127 (2018) 772–783, https://doi.org/10.1016/j.ijheatmasstransfer.2018.07.044.
- [29] Q. Ma, X. Wu, T. Li, Droplet impact on superheated surfaces with different wettabilities, Int. J. Heat Mass Transf. 141 (2019) 1181–1186, https://doi.org/10.1016/ j.ijheatmasstransfer.2019.07.027.
- [30] M. Zhang, J. Zhu, Z. Tao, L. Qiu, A quantitative phase diagram of droplet impingement boiling, Int. J. Heat Mass Transf. 177 (2021), https://doi.org/10.1016/j. ijheatmasstransfer.2021.121535.
- [31] T. Tran, H.J. Staat, A. Prosperetti, C. Sun, D. Lohse, Drop impact on superheated surfaces, Phys. Rev. Lett. 108 (2012), https://doi.org/10.1103/PhysRevLett.108. 036101
- [32] V. Bertola, An impact regime map for water drops impacting on heated surfaces, Int. J. Heat Mass Transf. 85 (2015) 430–437, https://doi.org/10.1016/j.iiheatmasstransfer.2015.01.084.
- [33] I.V. Roisman, J. Breitenbach, C. Tropea, Thermal atomisation of a liquid drop after impact onto a hot substrate, J. Fluid Mech. 842 (2018) 87–101, https://doi.org/10. 1017/jfm.2018.123.

- [34] C.E. Clavijo, J. Crockett, D. Maynes, Hydrodynamics of droplet impingement on hot surfaces of varying wettability, Int. J. Heat Mass Transf. 108 (2017) 1714–1726, https://doi.org/10.1016/J.IJHEATMASSTRANSFER.2016.12.076.
- [35] G.E. Cossali, M. Marengo, M. Santini, Secondary atomisation produced by single drop vertical impacts onto heated surfaces, Exp. Therm. Fluid Sci. 29 (2005) 937–946, https://doi.org/10.1016/j.expthermflusci.2004.12.003.
- [36] C.E. Clavijo, K. Stevens, J. Crockett, D. Maynes, Thermally induced atomization during droplet impingement on superheated hydrophobic and superhydrophobic surfaces, Int. J. Heat Mass Transf. 126 (2018) 1357–1366, https://doi.org/10.1016/ j.ijheatmasstransfer.2018.05.068.
- [37] M. Reyssat, A. Pépin, F. Marty, Y. Chen, D. Quéré, Bouncing transitions on microtextured materials, Europhys. Lett. 74 (2006) 306–312, https://doi.org/10.1209/epl/ i2005-10523-2.
- [38] C. Yadav, R.R. Sahoo, Thermophysical properties and thermal performance evaluation of multiwalled carbon nanotube-based organic phase change materials using t-history method, Int. J. Energy Res. 46 (2022) 3115–3131, https://doi.org/10.1002/er.7368.